

# Compressibility and equation of state of beryl ( $\text{Be}_3\text{Al}_2\text{Si}_6\text{O}_{18}$ ) by using a diamond anvil cell and in situ synchrotron X-ray diffraction

Dawei Fan<sup>1,2</sup> · Jingui Xu<sup>1,3</sup> · Yunqian Kuang<sup>1,3</sup> · Xiaodong Li<sup>4</sup> · Yanchun Li<sup>4</sup> · Hongsen Xie<sup>1</sup>

Received: 13 December 2014 / Accepted: 16 March 2015 / Published online: 26 March 2015  
© Springer-Verlag Berlin Heidelberg 2015

**Abstract** High-pressure single-crystal synchrotron X-ray diffraction was carried out on a single crystal of natural beryl compressed in a diamond anvil cell. The pressure–volume ( $P$ – $V$ ) data from room pressure to 9.51 GPa were fitted by a third-order Birch–Murnaghan equation of state (BM-EoS) and resulted in unit-cell volume  $V_0 = 675.5 \pm 0.1 \text{ \AA}^3$ , isothermal bulk modulus  $K_0 = 180 \pm 2 \text{ GPa}$ , and its pressure derivative  $K'_0 = 4.2 \pm 0.5$ . We also calculated  $V_0 = 675.5 \pm 0.1 \text{ \AA}^3$  and  $K_0 = 181 \pm 1 \text{ GPa}$  with fixed  $K'_0$  at 4.0 and then obtained the axial moduli for  $a$  ( $K_{a0}$ )-axis and  $c$  ( $K_{c0}$ )-axis of  $209 \pm 1$  and  $141 \pm 2 \text{ GPa}$  by “linearized” BM-EoS approach. The axial compressibilities of  $a$ -axis and  $c$ -axis are  $\beta_a = 1.59 \times 10^{-3} \text{ GPa}^{-1}$  and  $\beta_c = 2.36 \times 10^{-3} \text{ GPa}^{-1}$  with an anisotropic ratio of  $\beta_a:\beta_c = 0.67:1.00$ . On the other hand, the pressure–volume–temperature ( $P$ – $V$ – $T$ ) EoS of the natural beryl has also been measured at temperatures up to 750 K and at pressures up to 16.81 GPa, using diamond anvil cell in conjunction with in situ synchrotron angle-dispersive powder X-ray diffraction. The  $P$ – $V$  data at room temperature and at a pressure range of 0.0001–15.84 GPa were then analyzed by third-order BM-EoS and yielded  $V_0 = 675.3 \pm 0.1 \text{ \AA}^3$ ,  $K_0 = 180 \pm 2 \text{ GPa}$ ,

$K'_0 = 4.2 \pm 0.3$ . With  $K'_0$  fixed to 4.0, we also obtained  $V_0 = 675.2 \pm 0.1 \text{ \AA}^3$  and  $K_0 = 182 \pm 1 \text{ GPa}$ . Consequently, we fitted the  $P$ – $V$ – $T$  data with high-temperature BM-EoS approach using the resultant  $K'_0$  (4.2) from room-temperature BM-EoS and then obtained the thermoelastic parameters of  $V_0 = 675.3 \pm 0.2 \text{ \AA}^3$ ,  $K_0 = 180 \pm 1 \text{ GPa}$ , temperature derivative of the bulk modulus  $(\partial K/\partial T)_p = -0.017 \pm 0.004 \text{ GPa K}^{-1}$ , and thermal expansion coefficient at ambient conditions  $\alpha_0 = (2.82 \pm 0.74) \times 10^{-6} \text{ K}^{-1}$ . Present results were also compared with previous studies for beryl. From the comparison of these fittings, we propose to constrain  $K_0 = 180 \text{ GPa}$  and  $K'_0 = 4.2$  for beryl. And we also observed that beryl exhibits anisotropic thermal expansion at relatively low temperatures, which is very consistent with previous studies. Furthermore, no phase transition was observed in the entire pressure and temperature range (up to 16.84 GPa and 750 K) of this study for the natural beryl.

**Keywords** Beryl · Equation of state · High pressure and high temperature · X-ray diffraction · Diamond anvil cell

## Introduction

Beryl, a beryllium aluminum silicate mineral, is mostly found in granites and granite pegmatites (Charoy 1999; Evensen et al. 1999) and sometimes in topaz rhyolite, metamorphic rocks, or in the veins and cavities of limestones and marbles (Evensen et al. 1999). The occurrence of beryl rather than other beryllium silicate minerals in granitic pegmatites stems from its stability relations in quartz-saturated portions of the system  $\text{BeO}$ – $\text{Al}_2\text{O}_3$ – $\text{SiO}_2$ – $\text{H}_2\text{O}$  (Burt 1978; Barton 1986; Čemić et al. 1986; Evensen et al. 1999), in which divariant assemblages containing beryl + quartz occur over the range of moderate pressures

✉ Dawei Fan  
fandawei@vip.gyig.ac.cn

<sup>1</sup> Key Laboratory for High Temperature and High Pressure Study of the Earth's Interior, Institute of Geochemistry, Chinese Academy of Sciences, Guiyang 550002, China

<sup>2</sup> Center for High Pressure Science and Technology Advanced Research, Changchun 130012, China

<sup>3</sup> University of Chinese Academy of Sciences, Beijing 100049, China

<sup>4</sup> Beijing Synchrotron Radiation Facility, Institute of High Energy Physics, Chinese Academy of Sciences, Beijing 100049, China

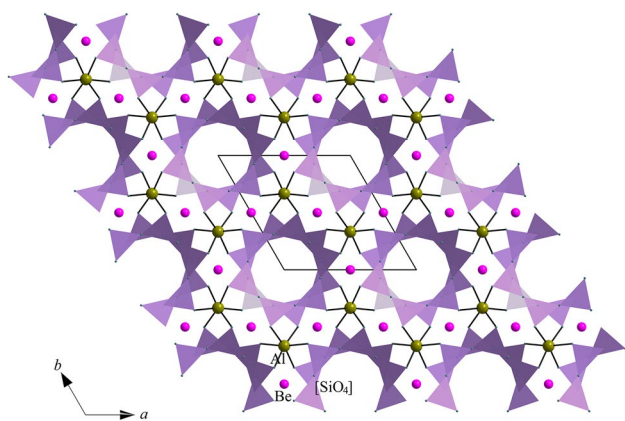


**Fig. 1** Single-crystal structure of beryl viewed down [001] at ambient conditions (*color online*)

and temperatures pertinent to the magmatic consolidation of pegmatites (Evensen et al. 1999). The tetrahedral framework of beryl (ideal formula  $\text{Be}_3\text{Al}_2\text{Si}_6\text{O}_{18}$ ; space group  $P6/mcc$ ) is composed of sixfold rings of Si tetrahedral cross-linked by Be-containing tetrahedral and Al-containing octahedral polyhedra (Fig. 1). The stacking of the sixfold ring gives rise to open channels that aligned along the  $c$ -axis (Gibbs et al. 1968). Previous studies on composition and structure have shown that the open channels in the beryl structure can accommodate water molecules as well as alkali cations (Gibbs et al. 1968; de Almeida Sampaio Filho et al. 1973a, b; Hawthorne and Černý 1977; Goldman et al. 1978; Aines and Rossman 1984; Brown and Mills 1986; Adamo et al. 2008). The presence of alkali cations is generally ascribed to the balance on the deficiency of positive charges, resulting from the replacement of octahedral Al and tetrahedral Be by cations of lower valence, such as  $\text{Fe}^{2+}$ ,  $\text{Mn}^{2+}$ ,  $\text{Mg}^{2+}$ , and  $\text{Li}^+$ . (Aurisicchio et al. 1988). And the beryl mineral shows variations of physical properties because of a very complex crystal-chemical behavior (Aurisicchio et al. 1988). Therefore, the accurate knowledge of the physical properties (such as thermoelastic properties) of beryl at high pressure and high temperature is essential to understand the geochemical behavior of beryllium at high pressure and high temperature and the hydroxyl occurrence in nominally anhydrous phases in the Earth's interior.

To date, several studies have been carried out on the crystal-chemistry behavior of beryls and devoted to determining the position and orientation of water molecule inside the channels of the structure with a wide variety of extra-framework populations (Wood and Nassau 1968; de Almeida Sampaio Filho et al. 1973a, b; Goldman et al. 1978; Aines and Rossman 1984; Barton 1986; Brown and Mills 1986; Čemić et al. 1986; Hazen et al. 1986; Aurisicchio et al. 1988; Sheriff et al. 1991; Artioli et al. 1993; Charoy et al. 1996; Kolesov and Geiger 2000; Pankrath and

Langer 2002; Andersson 2006; Gatta et al. 2006; Adamo et al. 2008). However, there are few reports in the literature about the elasticity of beryl at high pressure (Yoon and Newnham 1973; Hazen et al. 1986; Prencipe and Nestola 2005; Qin et al. 2008), especially for the thermoelasticity of beryl at simultaneously high pressure and high temperature (Prencipe et al. 2011). Hazen et al. (1986) investigated the compressibility and high-pressure behavior of beryl at high pressure up to 6 GPa using a diamond anvil cell and obtained the value of  $170$  (5) GPa for bulk modulus  $K_0$  under the assumption of its pressure derivative ( $K'_0$ ) to be 4. Similarly, Prencipe and Nestola (2005) also investigated the compressive behavior of beryl at room temperature and high pressure up to 6.3 GPa and gave the bulk modulus  $K_0 = 179 \pm 1$  GPa and its pressure derivative  $K'_0 = 3.7 \pm 0.3$  GPa. Subsequently, Qin et al. (2008) studied the compression behavior of beryl up to 19.2 GPa, using diamond anvil cell in conjunction with in situ synchrotron radiation energy-dispersive X-ray diffraction, and obtained the  $K_0$  value as  $226 \pm 6$  GPa with fixed  $K'_0$  at 4. Their calculations are different from both results obtained by Hazen et al. (1986) ( $K_0 = 170 \pm 5$  GPa) and by Prencipe and Nestola (2005) ( $K_0 = 179 \pm 1$  GPa).

Recently, Prencipe et al. (2011) examined the thermoelastic properties of beryl by means of ab initio calculations (B3LYP and WC1LYP Hamiltonians) and provided the  $K_0$  as a value of 180 GPa. Their resultant bulk modulus is in reasonable agreement with those in the studies of Hazen et al. (1986) (170 GPa) and Prencipe and Nestola (2005) (179 GPa) under uncertainties, but is far different from the results of Qin et al. (2008) (226 GPa). Additionally, Prencipe et al. (2011) predicted a phase transition of zone-center soft mode from  $P6/mcc$  to  $P\bar{1}$  at a pressure about 14 GPa by theoretical calculation. However, Qin et al. (2008) stated that no evidence for the phase transition of beryl was observed in the range of experimental pressure up to 19.2 GPa. Therefore, it is necessary to carry out the thermoelastic properties of beryl by in situ experiments at simultaneously high-pressure and high-temperature conditions to clarify the accurate thermoelasticity as well as the evidence of phase transition for further discussion.

Even though recent theoretical studies, based on ab initio calculations (Prencipe et al. 2011), give new insights into the thermoelastic properties of beryl at simultaneously high pressure and high temperature, no experimental data of unit-cell parameters and structures at high pressure and high temperature are yet obtained to define the thermoelastic properties of beryl. With the improvement in synchrotron facilities and other state-of-arts techniques, we are now able to obtain more accurate and precise data to reinvestigate the thermoelasticity of beryl at simultaneously high pressure and high temperature. Hence, we have investigated the  $P$ - $V$ - $T$  relations of a natural beryl at high

pressure and high temperature, using a diamond anvil cell combined with in situ synchrotron radiation angle-dispersive X-ray diffraction. In this study, the thermoelastic properties of beryl are derived by applied the  $P$ – $V$ – $T$  data to the high-temperature BM-EoS. Our results are also discussed with those elastic and thermoelastic properties of beryl reported in the literatures.

## Sample and experimental methods

### Sample

A natural, colorless, transparent, gem-quality single-crystal beryl sample from Aletai of Xinjiang Region, China, was selected for this investigation. The pure beryl mineral grains were selected by hand under a microscope, some grains were used for the high-pressure single-crystal X-ray diffraction experiments, and the others then grounded in an agate mortar for 4–6 h to an average grain size of  $\sim 10 \mu\text{m}$ . The ground samples were examined using the conventional powder X-ray diffraction method, after being heated at  $50^\circ\text{C}$  in a constant temperature furnace for 2 h to eliminate the absorbed water. The ambient X-ray diffraction data were collected using a D/Max-2200 X-ray diffractometer with graphite crystal monochromator and  $\text{Cu K}\alpha$  radiation. The ambient X-ray spectrum of beryl sample was indexed according to the standard spectra that confirmed the structure of the natural beryl sample is hexagonal and belongs to the  $P6/mcc$  space group with the unit-cell parameters of  $a = 9.2043 \pm 0.0005 \text{ \AA}$ ,  $c = 9.2103 \pm 0.0006 \text{ \AA}$ ,  $V = 675.75 \pm 0.22 \text{ \AA}^3$ ,  $c/a = 1.0007$ . According to the Aurisicchio et al. (1988) definition, based on the relationship between  $c/a$  ratio and chemical composition, our sample belongs to the “tetrahedral beryl group.”

### Room-temperature and high-pressure single-crystal X-ray diffraction experiment

Before loading in the diamond anvil cell, the crystal was examined in air. Refined unit-cell parameters constrained to hexagonal symmetry are reported in Table 1. The in situ room-temperature and high-pressure synchrotron single-crystal X-ray diffraction experiments were carried out at BL15U1 beamline using angle-dispersive diffraction with diamond anvil cells at the Shanghai Synchrotron Radiation Facility (SSRF). A symmetric-type diamond anvil cell equipped with  $500\text{-}\mu\text{m}$  diamond culets was used. Gaskets made from stainless-steel foil (type T301), pre-indented to a thickness of  $\sim 55 \mu\text{m}$ , and then drilled to a diameter of  $200 \mu\text{m}$ , served as the sample chamber. The 4:1 methanol–ethanol mixture was used as pressure-transmitting medium, which is hydrostatic up to 10 GPa

**Table 1** Unit-cell parameters of beryl from single-crystal X-ray diffraction data at high pressure and room temperature

$P$ (GPa)	$a$ (Å)	$c$ (Å)	$V$ (Å <sup>3</sup> )	$c/a$
0.0001	9.2042(1)	9.2104(2)	675.73(15)	1.0007(1)
0.20(1)	9.2012(3)	9.2041(5)	674.84(19)	1.0003(1)
0.75(4)	9.1938(5)	9.1926(3)	672.91(22)	0.9999(1)
1.22(6)	9.1865(6)	9.1846(7)	671.26(25)	0.9998(1)
1.85(9)	9.1786(5)	9.1691(6)	668.97(18)	0.9990(1)
2.41(12)	9.1701(5)	9.1614(5)	667.18(26)	0.9991(1)
2.97(15)	9.1628(4)	9.1487(7)	665.19(22)	0.9985(1)
3.94(20)	9.1492(3)	9.1283(8)	661.74(15)	0.9977(2)
4.63(23)	9.1394(3)	9.1174(6)	659.53(22)	0.9976(2)
5.35(27)	9.1287(3)	9.1020(6)	656.88(24)	0.9971(1)
6.41(32)	9.1167(4)	9.0830(8)	653.79(19)	0.9963(1)
7.30(37)	9.1041(3)	9.0642(7)	650.63(20)	0.9956(1)
7.89(39)	9.0976(5)	9.0555(8)	649.08(15)	0.9954(2)
8.42(42)	9.0903(8)	9.0469(6)	647.42(22)	0.9952(1)
9.51(48)	9.0777(5)	9.0305(8)	644.46(19)	0.9948(2)

Numbers in parenthesis represent standard deviations

as demonstrated by Piermarini et al. (1973) and Angel et al. (2007). Ruby chip was loaded as pressure calibrant together with the beryl sample ( $50 \times 50 \times 25 \mu\text{m}$ ) in the pre-indented T301 stainless-steel gasket with a  $200\text{-}\mu\text{m}$  sample hole. Ruby fluorescence spectra were collected before and after each collection of data, and the positions of the R1 and R2 peaks were determined by fitting with Lorentzian functions. Pressure was calculated from the fitted R1 and R2 peak positions using the method of Mao et al. (1978). Diffraction images were collected using MAR-165 charge-coupled device (CCD) detector, placed at a sample-to-detector distance of approximately 180 mm. The detector geometry parameters were calibrated with  $\text{CeO}_2$  diffraction standard. The X-ray beam was monochromatized to a wavelength of  $0.6199 \text{ \AA}$  and focused down to  $2 \times 3 \mu\text{m}^2$  area. Data were collected rotating the diamond anvil cell for  $24^\circ$  round the vertical axis of the instrument ( $\omega$ -axis, from  $-12^\circ$  to  $+12^\circ$ ), with a typical exposure time of 0.5 s/deg. Diffraction images were analyzed using the GSE\_ADA/RSV software package (Dera et al. 2013). Then, the unit-cell parameters of beryl were calculated by least-squares technique using Unitcell program (Holland and Redfern 1997). Each diffraction pattern has at least 30 good single-crystal diffraction spots. In addition, besides the single-crystal diffraction spots of diamond, all the other single-crystal diffraction spots could be successfully indexed using the hexagonal symmetry of beryl. In the calculation, at least 11 sample diffraction spots [(100), (110), (200), (210), (211), (310), (311), (320), (400), (410), and (411)] were used to refine the unit-cell parameters.

## High-temperature and high-pressure powder X-ray diffraction experiment

High-temperature and high-pressure experiments were carried out by using a modified Merrill–Bassett-type diamond anvil cell. A pair of 500- $\mu\text{m}$ -culet-size diamond anvil was used. Gaskets made from stainless-steel foil (type T301), pre-indented to a thickness of  $\sim 50\ \mu\text{m}$ , and then drilled to a diameter of 200  $\mu\text{m}$ , served as the sample chamber. The beryl sample powders were slightly pressed between two opposing diamond anvils to form an approximately 25- $\mu\text{m}$ -thick disk, and a piece of beryl sample about 100  $\mu\text{m}$  in diameter was loaded into the sample chamber. The cell pressure was determined using the equation of state of gold (pressure marker) as proposed by Fei et al. (2007). The pressure-transmitting medium was a 4:1 mixture methanol–ethanol. Heating was carried out by using a resistance-heating system, and the temperature was measured by a Pt<sub>90</sub>Rh<sub>10</sub>–Pt<sub>100</sub> thermocouple, which was attached to the pavilion of the diamond. We first compressed the sample up to 10 GPa and then increased the temperature up to 750 K. Heating was maintained at 750 K for several minutes in order to minimize the effect of non-hydrostatic stress that could develop upon cold compression. Following this, the temperature was lowered down to 300 K in 150 K steps. For each P–T condition, an X-ray diffraction pattern was collected. The spectrums were selected after the experiment temperature was kept for  $\sim 600$  s. Typical exposure times for collecting diffraction patterns of the sample and the pressure marker were 600 s. Details of the experimental setup and cell assembly were described in Fan et al. (2010).

In situ high-temperature and high-pressure angle-dispersive X-ray powder diffraction experiments were conducted at the 4W2 beamline of the Beijing Synchrotron Radiation Facility (BSRF). An image plate detector (MAR-345) was used to collect diffraction patterns. The wavelength of the monochromatic X-ray beam is 0.6199 Å calibrated by scanning through the Mo metal *K*-absorption edge. The X-ray beam was focused to a beam size of  $20 \times 30\ \mu\text{m}^2$  full width at half maximum (FWHM) by a pair of Kirkpatrick–Baez mirrors. The tilting and rotation of the detector relative to the incident X-ray beam were calibrated using cerium dioxide (CeO<sub>2</sub>) powder as the X-ray diffraction standard. The sample-detector distance was calculated from the powder CeO<sub>2</sub> diffraction pattern at ambient conditions. The collected diffraction patterns were integrated to generate the conventional one-dimensional diffraction profiles using the Fit2D program (Hammersley et al. 1996). Figure 2 shows a typical fitting of the full X-ray diffraction pattern at 10.63 GPa and 750 K for beryl. Analyzes of all the patterns were carried out by means of the full profile-fitting technique implemented in the EXPGUI/GSAS

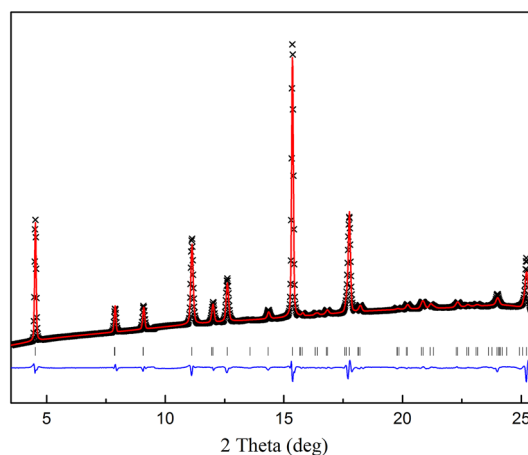


**Fig. 2** Le Bail profile fitting of the diffraction profiles at 10.63 GPa and 750 K of beryl. Observed spectra (*black line*), fitted spectra (*red solid line*), difference plot (*blue solid line*), and Bragg peak positions (*tick marks*) are shown (*color online*)

software package (Larson and Von Dreele 2000; Toby 2001). Refinement of peak positions and extraction of cell parameters were achieved by reducing full diffraction patterns following the Le Bail method (Le Bail et al. 1988). Precision upon the volume for beryl was estimated from the full spectrum fitting (Le Bail refinement) of X-ray diffraction profiles.

## Results and discussion

Unit-cell parameters of beryl at various pressures and temperatures conditions were refined from single-crystal and powder X-ray diffraction as shown in Tables 1 and 2, respectively. The X-ray diffraction patterns collected for the beryl sample showed that no phase transformation was observed throughout the whole range of pressure and temperature performed in these experiments (Fig. 3). This result in this study is very consistent with those collected with X-ray diffraction method in the study of Hazen et al. (1986) and Qin et al. (2008), whereas it is different with the conclusions made by Prencipe et al. (2011) in terms of ab initio calculation method that Prencipe et al. (2011) predicted a phase transition of zone-center soft mode from *P6/mcc* to *P1* will occur at a pressure about 14 GPa. Furthermore, for the room-temperature and high-pressure single-crystal X-ray diffraction data, we fitted the *P*–*V* data to the third-order BM-EoS to derive the elastic parameters of beryl. On the other hand, we firstly fitted the compression *P*–*V* data at the 300 K isotherm to the BM-EoS to derive the elastic parameters and then applied the high-temperature BM-EoS approach to derive the thermoelastic parameters from the measured *P*–*V*–*T* data.

**Table 2** Unit-cell parameters of beryl from powder X-ray diffraction data at various pressure–temperature conditions

<i>P</i> (GPa)	<i>T</i> (K)	<i>V</i> (Å <sup>3</sup> )	<i>a</i> (Å)	<i>c</i> (Å)	<i>c/a</i>
0.0001	300	675.75(22)	9.2043(5)	9.2103(6)	1.0007(1)
0.08(2)	300	674.86(53)	9.2005(15)	9.2058(16)	1.0006(1)
0.17(6)	300	674.45(52)	9.1991(21)	9.2031(22)	1.0004(1)
0.78(8)	300	672.72(45)	9.1926(15)	9.1925(17)	1.0000(2)
2.05(11)	300	667.80(48)	9.1724(13)	9.1654(14)	0.9992(1)
2.92(13)	300	664.63(43)	9.1597(14)	9.1472(18)	0.9986(2)
3.29(12)	300	663.53(54)	9.1565(16)	9.1384(16)	0.9980(1)
4.23(23)	300	660.21(43)	9.1416(17)	9.1224(20)	0.9979(2)
5.04(25)	300	657.42(54)	9.1314(18)	9.1041(18)	0.9970(1)
5.56(33)	300	656.21(56)	9.1258(15)	9.0986(15)	0.9970(1)
6.44(34)	300	653.26(54)	9.1149(14)	9.0794(17)	0.9961(2)
8.61(37)	300	646.50(57)	9.0877(13)	9.0393(14)	0.9947(1)
9.83(44)	300	642.72(54)	9.0704(16)	9.0207(18)	0.9945(1)
12.91(47)	300	634.09(67)	9.0358(13)	8.9679(20)	0.9925(2)
14.53(45)	300	630.13(49)	9.0181(16)	8.9469(22)	0.9921(2)
15.84(49)	300	626.32(55)	9.0017(12)	8.9253(17)	0.9915(1)
2.94(22)	450	665.27(47)	9.1635(11)	9.1485(15)	0.9984(2)
4.71(25)	450	658.05(56)	9.1373(13)	9.1011(16)	0.9960(2)
7.14(28)	450	651.62(47)	9.1044(15)	9.0775(15)	0.9970(1)
8.15(32)	450	647.26(63)	9.0894(12)	9.0464(18)	0.9953(2)
10.72(36)	450	639.58(59)	9.0587(11)	8.9997(18)	0.9935(1)
12.31(38)	450	636.07(48)	9.0425(14)	8.9824(20)	0.9934(1)
14.46(43)	450	629.29(34)	9.0146(15)	8.9418(19)	0.9919(1)
16.81(48)	450	623.53(49)	8.9874(13)	8.9138(20)	0.9918(2)
3.26(11)	600	663.71(41)	9.1602(14)	9.1335(18)	0.9971(2)
4.44(17)	600	659.70(34)	9.1421(16)	9.1143(17)	0.9970(1)
7.33(22)	600	650.72(59)	9.1036(14)	9.0664(16)	0.9959(2)
10.92(26)	600	639.57(44)	9.0574(15)	9.0023(19)	0.9939(2)
13.49(37)	600	632.68(59)	9.0257(13)	8.9679(20)	0.9936(2)
14.13(41)	600	630.25(51)	9.0175(15)	8.9497(15)	0.9925(1)
16.74(47)	600	623.18(46)	8.9866(16)	8.9103(15)	0.9915(1)
3.49(16)	750	663.09(58)	9.1606(12)	9.1242(18)	0.9960(2)
4.52(20)	750	659.63(55)	9.1408(13)	9.1159(16)	0.9973(2)
7.06(24)	750	650.95(45)	9.1073(14)	9.0623(19)	0.9951(1)
10.63(35)	750	639.97(56)	9.0613(13)	9.0002(20)	0.9933(2)
13.43(41)	750	632.29(57)	9.0285(13)	8.9568(19)	0.9921(1)
15.77(47)	750	625.71(51)	9.0027(15)	8.9145(16)	0.9902(1)

Numbers in parenthesis represent standard deviations

### Single-crystal X-ray diffraction data at room temperature and high pressure

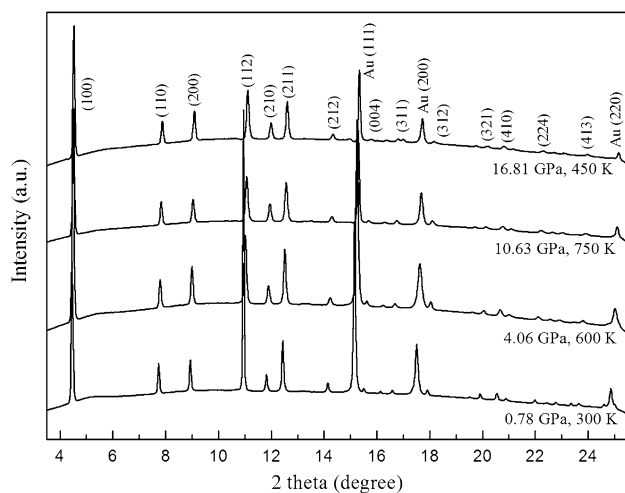
The pressure–volume (*P*–*V*) relations (Table 1) have been determined by fitting the present room-temperature single-crystal X-ray diffraction data to a third-order BM-EoS, which is represented as follows:

$$P = (3/2)K_0 \left[ (V_0 - V)^{7/3} - (V_0 - V)^{5/3} \right] \times \left\{ 1 + (3/4)(K'_0 - 4) \left[ (V_0 - V)^{2/3} - 1 \right] \right\} \quad (1)$$

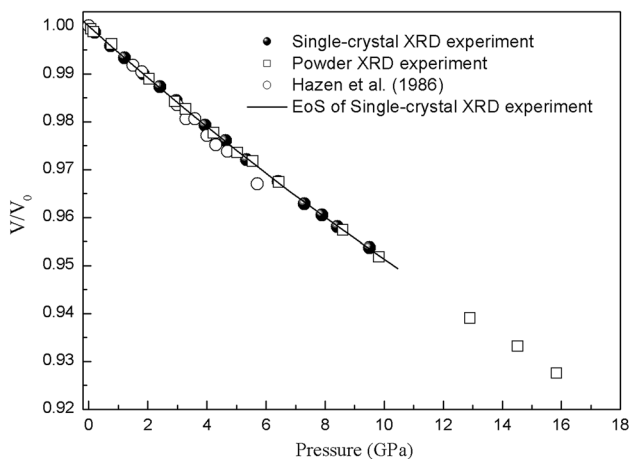
where  $V_0$ ,  $K_0$ , and  $K'_0$  are the unit-cell volume, isothermal bulk modulus, and its pressure derivative at ambient condition, respectively. Analyses of Eq. (1) with all parameters free yield  $V_0 = 675.5 \pm 0.1 \text{ \AA}^3$ ,  $K_0 = 180 \pm 2 \text{ GPa}$ ,  $K'_0 = 4.2 \pm 0.5$  for beryl. With fixed  $K'_0$  at 4, the fitting results yield  $V_0 = 675.5 \pm 0.1 \text{ \AA}^3$  and  $K_0 = 181 \pm 1 \text{ GPa}$ , respectively. Figure 4 shows the volume compression ( $V/V_0$ ) of beryl as a function of pressure (*P*) and derived equation of state and compares with the previous study by Hazen et al. (1986).

Figure 5 shows the volume Eulerian finite strain ( $f_E = [(V_0/V)^{2/3} - 1]$ ) versus “normalized pressure” ( $F_E = P/[3f_E(2f_E + 1)^{5/2}]$ ) plot ( $F_E - f_E$  plot; Angel 2000) of beryl in this study. The weighted linear regression through the data points yields the intercept value,  $F_E(0) = 179 \pm 2 \text{ GPa}$  for beryl, which shows an excellent agreement with the isothermal bulk modulus obtained by the third-order BM-EoS ( $180 \pm 2 \text{ GPa}$ ). Furthermore, it is clear from Fig. 5 that the normalized pressure as a function of the Eulerian strain at 300 K has a positive slope, which is consistent with a value of  $K'_0$  slightly larger than 4 (Angel 2000), shows that the third-order BM-EoS is a reasonable description of the *P*–*V* data in this study.

The unit-cell parameters as functions of pressure are summarized in Table 1 and plotted in Fig. 6. By fitting a “linearized” BM-EoS and following the procedure implemented in the EoSFit 5.2 program (Angel 2000), we can obtain the axial compressible modulus parameters ( $K_{a0} = 209 \pm 1 \text{ GPa}$  and  $K_{c0} = 141 \pm 2 \text{ GPa}$  for the *a*-axis and *c*-axis, respectively). Then, zero-pressure axial compressibilities from the beryl *P*–*V* experimental data were found to be  $1.59 \times 10^{-3}$  and  $2.36 \times 10^{-3} \text{ GPa}^{-1}$  for the *a*-axis and *c*-axis, respectively, and the anisotropic ratio of the *a*- and *c*-axis is  $\beta_a:\beta_c = 0.67:1.00$ . The axial compressibility of beryl in this study is in good agreement with previous studies, which showed that there has small axial compression anisotropy along *a*-axis and *c*-axis: The axial compressibility along *c*-axis is larger than along *a*-axis (Hazen et al. 1986; Yoon and Newnham 1973). There are two possible reasons for the axial compressibility along *c*-axis is larger than along *a*-axis. One is the incorporation of relatively larger molecular water in the *c*-parallel structural channels in beryl. Another reason is that *a*-axis mainly consists of the Si–O tetrahedron, while *c*-axis mainly consists of the Be–O tetrahedron and Al–O octahedron. And the variation of Si–O bonds and O–Si–O angles in the Si–O tetrahedron at high pressure is smaller than the Be–O bonds and O–Be–O angles in the Be–O tetrahedron, and the Al–O bonds and O–Al–O angles in the Al–O octahedron (Hazen et al., 1986).



**Fig. 3** Typical X-ray diffraction patterns of beryl from powder X-ray diffraction experiments at high pressure and high temperature



**Fig. 4** Volume compression of beryl at high pressure and room temperature from single-crystal X-ray diffraction experiments in this study compared with the results from powder X-ray diffraction experiments in this study and the previous study by Hazen et al. (1986). The third-order Birch–Murnaghan equation of state fitted with  $K_0$  and  $K'_0$  is 180 GPa and 4.2 for beryl in this study. The error bars of the data points are smaller than the symbols

### Powder X-ray diffraction data at high temperature and high pressure

#### Room-temperature BM-EoS

The  $P$ – $V$  data (Table 2) from powder X-ray diffraction experiments were also used to determine the elastic properties by fitting the present room-temperature powder X-ray diffraction data to a third-order BM-EoS. Analyses of Eq. (1) with all parameters free yield  $V_0 = 675.3 \pm 0.1 \text{ \AA}^3$ ,  $K_0 = 180 \pm 2 \text{ GPa}$ ,  $K'_0 = 4.2 \pm 0.3$  for beryl. With fixed  $K'_0$  at 4, the fitting results yield  $V_0 = 675.2 \pm 0.1 \text{ \AA}^3$  and

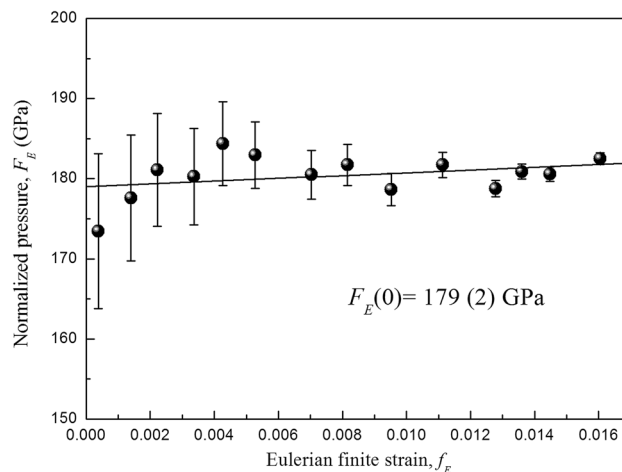


**Fig. 5** Volume Eulerian strain-normalized pressure ( $F_E - f_E$ ) plot of beryl. The solid line represents the linear fit through the data

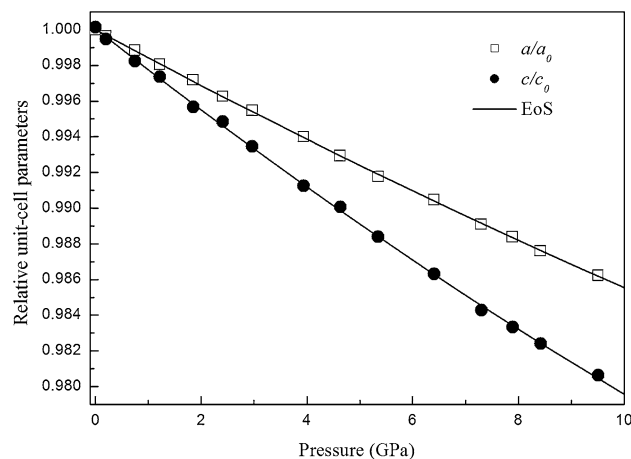


**Fig. 6** Axial compression  $a/a_0$ , and  $c/c_0$  as a function of pressure for beryl from single-crystal X-ray diffraction experiments in this study. Note that the symbols are larger than the uncertainties

$K_0 = 182 \pm 1 \text{ GPa}$ . Figure 4 also shows the volume compression ( $V/V_0$ ) of beryl as a function of pressure ( $P$ ) from powder X-ray diffraction experiments and compares with the results from single-crystal X-ray diffraction experiments and the previous study by Hazen et al. (1986). From Fig. 4 and Table 3, we can find that  $V_0$ ,  $K_0$ , and  $K'_0$  of beryl from powder X-ray diffraction data are in extreme agreement with the results from single-crystal X-ray diffraction data.

#### High-temperature BM-EoS

The  $P$ – $V$ – $T$  data (Table 2) from powder X-ray diffraction experiments were used to determine the thermoelastic properties of beryl up to  $\sim 17 \text{ GPa}$  and 750 K. The

**Table 3** Elastic and thermoelastic parameters of beryl with other beryllium silicate minerals

Sample	$K_0$ (GPa)	$K'_0$	$V_0$ (Å <sup>3</sup> )	$\alpha_0$ ( $\times 10^{-6}$ K <sup>-1</sup> )	$(\partial K/\partial T)_P$ (GPa K <sup>-1</sup> )	Methods	References
Beryl	180(2)	4.2(5)	675.5(1)	–	–	Single-XRD	This study
	181(1)	4.0 <sup>a</sup>	675.5(1)	–	–	Single-XRD	This study
	180(2)	4.2(3)	675.3(1)	–	–	Powder-XRD	This study
	182(1)	4.0 <sup>a</sup>	675.2(1)	–	–	Powder-XRD	This study
	180(1)	4.2 <sup>a</sup>	675.3(2)	2.82(74)	–0.017(4)	Powder-XRD	This study
	176	–	–	–	–	PSM	Yoon and Newnham (1973)
	181	3.90(5)	–	–	–	PSM	Yoon and Newnham (1973)
	170(5)	4.0 <sup>a</sup>	–	–	–	Single-XRD	Hazen et al. (1986)
	179(1)	3.7(3)	675.63(4)	–	–	Single-XRD	Prencipe and Nestola (2005)
	–	–	–	2.3	–	Single-XRD	Morosin (1972)
	180.2	4	–	–0.7	–0.020	WC1LYP	Prencipe et al. (2011)
	179.4	–	–	1.0	–	B3LYP	Prencipe et al. (2011)
Phenacite	–	–	–	16.8	–	XRD	Hazen and Finger (1987)

Numbers in parenthesis represent standard deviations

XRD, X-ray diffraction; PSM, Pulse-Superposition Method; WC1LYP, WC1LYP Hamiltonian method; B3LYP, B3LYP Hamiltonian method; Brillouin, Brillouin spectroscopy

<sup>a</sup> Fixed during fitting

high-temperature third-order BM-EoS was applied to our high-pressure and high-temperature data with the form as follows:

$$P = (3/2)K_{T0} \left[ (V_{T0} - V)^{7/3} - (V_{T0} - V)^{5/3} \right] \times \left\{ 1 + (3/4)(K'_{T0} - 4) \left[ (V_{T0} - V)^{2/3} - 1 \right] \right\} \quad (2)$$

In this equation, the thermal dependences of the zero-pressure volume  $V_{T0}$  and bulk modulus  $K_{T0}$  at different isotherms are expressed using the following equations:

$$V_{T0} = V_0 \exp \int_{300}^T \alpha_T dT \quad (3)$$

$$K_{T0} = K_0 + (\partial K_{T0}/\partial T)_P \times (T - 300) \quad (4)$$

where  $V_0$  is the volume at room pressure and temperature, and the temperature derivative for the unit-cell volume  $V_{T0}$  can be estimated by a function of the thermal expansion at ambient pressure  $\alpha_T$  (Eq. 3). The thermal dependence of the bulk modulus  $K_{T0}$  is expressed by a linear function of temperatures, temperature derivative  $(\partial K_{T0}/\partial T)_P$ , and  $K_0$  (Eq. 4).

The thermoelastic parameters  $\alpha_0$ ,  $(\partial K_T/\partial T)_P$ , and  $K_0$  of beryl obtained in this study are shown in Table 3. Fitting of the present  $P$ – $V$ – $T$  data to the high-temperature BM-EoS yields  $V_0 = 675.3 \pm 0.2$  Å<sup>3</sup>,  $K_0 = 180 \pm 1$  GPa,  $(\partial K/\partial T)_P = -0.017 \pm 0.004$  GPa K<sup>-1</sup>, and  $\alpha_0 = (2.82 \pm 0.74) \times 10^{-6}$  K<sup>-1</sup>, with fixed  $K'_0$  at 4.2, which obtained from room-temperature BM-EoS. The  $K_0$  determined here are consistent with the values derived from fitting of our  $P$ – $V$  data at 300 K within uncertainties. We

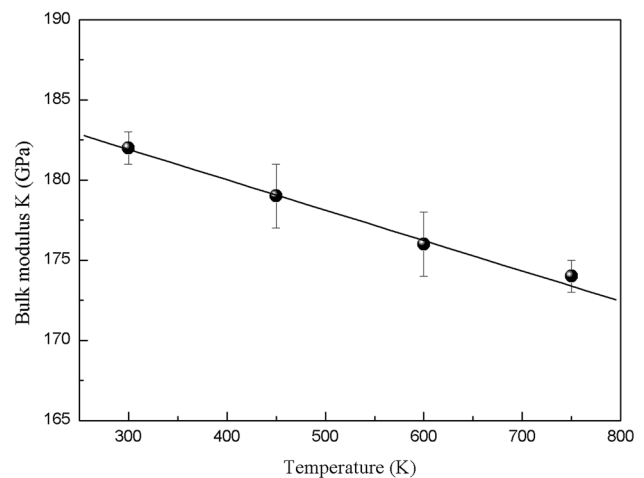


**Fig. 7** Variations of the isothermal bulk modulus of beryl against temperature. *Solid circles* denote the isothermal bulk moduli calculated by fitting the data at each temperature. The *solid line* represents the fitting to the HTBM EoS (Table 3)

also calculated the temperature derivative of bulk modulus extracted from each isotherm and obtained  $(\partial K_T/\partial T)_P = 0.018 \pm 0.005$  GPa K<sup>-1</sup> for beryl (Fig. 7), which are very consistent to the results from the whole set of  $P$ – $V$ – $T$  data available in this study ( $(\partial K_T/\partial T)_P = -0.017 \pm 0.004$  GPa K<sup>-1</sup>) within their uncertainties.

The methanol–ethanol mixture with 4:1 was used for the pressure medium in this study, which freezes above 10 GPa, and the hydrostatic circumstance of sample chamber will be influenced (Piermarini et al. 1973; Angel et al. 2007). However, the sample chamber in this study has been

heated up to 750 K at pressure higher than 10 GPa for the relaxation of the deviatoric stress. Although the effect of deviatoric stress on the unit-cell volume measurements should be small, we still need to assess the impact of non-hydrostatic compression to the thermoelastic parameters in this study. Likewise, fitting of the  $P$ – $V$ – $T$  data at pressures below ~10 GPa to the high-temperature BM-EoS yields  $V_0 = 675.3 \pm 0.1 \text{ \AA}^3$ ,  $K_0 = 179 \pm 2 \text{ GPa}$ ,  $(\partial K/\partial T)_P = -0.017 \pm 0.005 \text{ GPa K}^{-1}$ , and  $\alpha_0 = (2.74 \pm 0.85) \times 10^{-6} \text{ K}^{-1}$  with fixed  $K'_0$  at 4.2. These values are very consistent with the results of fitting all the  $P$ – $V$ – $T$  data that lead to  $V_0 = 675.3 \pm 0.2 \text{ \AA}^3$ ,  $K_0 = 180 \pm 1 \text{ GPa}$ ,  $(\partial K/\partial T)_P = -0.017 \pm 0.004 \text{ GPa K}^{-1}$ , and  $\alpha_0 = (2.82 \pm 0.74) \times 10^{-6} \text{ K}^{-1}$  within their uncertainties. This indicates that the impact of non-hydrostatic compression to thermoelastic parameters is very limited in this study.

In addition, the results for beryl show anisotropic elasticity along the  $a$ -axis and the  $c$ -axis with increasing pressure, and almost isotropic elasticity along the  $a$ -axis and the  $c$ -axis with increasing temperature at high pressure, as also illustrated in Fig. 8. The ratios of  $c/a$  generally decrease with increasing pressure, which means that the  $c$ -axis is more compressible under pressure when compared with the  $a$ -axis. This is very consistent with the results from the single-crystal X-ray diffraction data available in this study, which also shows that the axial compressibility along  $c$ -axis is larger than along  $a$ -axis. Furthermore, it appears that the temperature dependence of the ratios of  $c/a$  also remains stable with varying pressure. The ratios of  $c/a$  remain relatively unchanged with increasing temperature at high pressure, which means that the thermally expandable along  $c$ -axis is almost consistent with  $a$ -axis at high pressure.

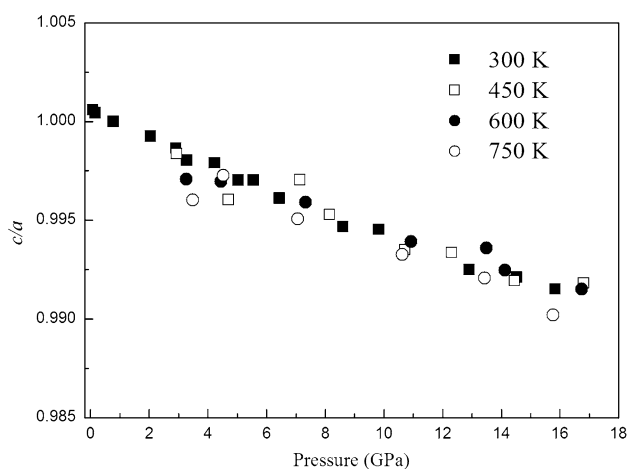


**Fig. 8** Variation of the  $c/a$  ratio for beryl with pressure and temperature in this study. The error bars of the data points are smaller than the symbols

## Comparison with previous studies of beryl

Elastic properties of beryl have been investigated by some authors. Table 3 summarizes the bulk moduli and their pressure derivatives for beryl determined by various experimental and theoretical techniques. As shown in Table 3, the  $K_0$  values of beryl from the literatures exhibit slightly discrepancies with each other, ranging from 170 to 181 GPa. In addition, the current results compared with previous studies for beryl are also shown in Table 3. Yoon and Newnham (1973) measured the second-order adiabatic elastic stiffnesses of beryl at ambient condition by using the pulse-superposition method and gave the bulk modulus  $K_0 = 181 \text{ GPa}$  and the pressure derivative of the bulk modulus  $K'_0 = 3.90 \pm 0.05$ . Subsequently, Hazen et al. (1986) determined the compressibility and high-pressure crystal structure of beryl by using X-ray diffraction methods and presented a slightly different result ( $K_0 = 170 \pm 5 \text{ GPa}$ ) with this study ( $K_0 = 180 \pm 2 \text{ GPa}$ ) and Yoon and Newnham (1973) ( $K_0 = 181 \text{ GPa}$ ). However, Prencipe and Nestola (2005) also investigated the compressive behavior of beryl at room temperature and high pressure using single-crystal X-ray diffraction method and obtained  $K_0 = 179 \pm 1 \text{ GPa}$  for beryl, which is very consistent with the results in this study and Yoon and Newnham (1973) within their uncertainties. Prencipe et al. (2011) investigated the thermoelastic properties of beryl at the hybrid HF/DFT level by using the ab initio calculation methods (B3LYP and WC1LYP Hamiltonians). The ab initio calculation from Prencipe et al. (2011) successfully reproduced the available experimental data concerning compressibility at room temperature, and B3LYP and WC1LYP Hamiltonian provided  $K_0$  values of 179.4 and 180.2 GPa, respectively. Hence, the bulk modulus of beryl obtained in this study is also in good agreement with previous studies by ab initio calculation methods within their uncertainties (Prencipe and Nestola 2005; Prencipe et al. 2011).

Furthermore, the results about the pressure derivative of bulk modulus for beryl in this study are also summarized in Table 3 and compared with data from previous studies. From the results, we conclude that  $K'_0$  for beryl from the single-crystal X-ray diffraction experiments ( $K'_0 = 4.3$ ) and powder X-ray diffraction experiments ( $K'_0 = 4.2$ ) is entirely identical within the fitting error in this study. In addition, the values of the pressure derivative of bulk modulus for beryl in previous studies are  $K'_0 = 3.90 \pm 0.05$  from Yoon and Newnham (1973) and  $K'_0 = 3.7 \pm 0.3$  from Prencipe and Nestola (2005). Therefore, the values of the pressure derivative of bulk modulus for beryl in this study are also in excellent agreement with previous studies for which were proposed that  $K'_0$  is close to 4.0 (Yoon and Newnham 1973; Hazen et al. 1986; Prencipe and Nestola 2005; Prencipe

et al. 2011). Therefore, from the comparison of this study with previous results, we can propose to constrain the bulk modulus and its pressure derivative to  $K_0 = 180$  GPa and  $K'_0 = 4.2$  for beryl.

Table 3 also summarizes the thermal expansion coefficient and temperature derivative of the bulk modulus at ambient conditions of beryl in this study compared with the previous studies. The temperature derivative of the bulk modulus of beryl obtained from X-ray diffraction method in this study ( $(\partial K/\partial T)_p = -0.017$  GPa K<sup>-1</sup>) is very consistent with the result ( $(\partial K/\partial T)_p = -0.020$  GPa K<sup>-1</sup>) from ab initio calculation method by Prencipe (2011). In addition, Morosin (1972) measured the lattice constants of beryl at room pressure and high temperature over the temperature range 300–1100 K using a high-temperature single-crystal furnace and derived that the thermal expansion coefficient of beryl at ambient conditions is  $2.3 \times 10^{-6}$  K<sup>-1</sup>. Therefore, the thermal expansion coefficient at ambient conditions of beryl obtained in this study ( $\alpha_0 = 2.82 \times 10^{-6}$  K<sup>-1</sup>) is in good agreement with the result from the work of Morosin (1972) within their uncertainties. Similarly, Prencipe et al. (2011) also determined the thermal expansion coefficient of beryl by using ab initio calculation method (B3LYP and WC1LYP methods) at high pressure (up to 6 GPa) and three different temperatures (300, 600, and 900 K); the B3LYP gives that the thermal expansion coefficient at ambient conditions of beryl is  $1.0 \times 10^{-6}$  K<sup>-1</sup>, whereas the WC1LYP gives that the thermal expansion coefficient at ambient conditions of beryl is  $-0.7 \times 10^{-6}$  K<sup>-1</sup>. The B3LYP calculated thermal expansion coefficient at ambient conditions appears to be in closer agreement with the experimental data than the WC1LYP one (Prencipe et al. 2011). We also compared the thermal expansion coefficient at ambient conditions of beryl in this study with the result for phenacite from Hazen and Finger (1987), which reported that the thermal expansion coefficient at ambient conditions of phenacite is  $16.8 \times 10^{-6}$  K<sup>-1</sup> by using X-ray diffraction methods at several temperatures up to about 1000 K and room pressure. From Table 3, we can find that the thermal expansion coefficient at ambient conditions between beryl and phenacite is quite different. We infer that the main reason maybe the different axial anisotropic thermal expansion along *a*-axis and *c*-axis between beryl and phenacite. Phenacite has slightly anisotropic thermal expansion: The axial thermal expansivities of phenacite at ambient conditions along *a*-axis and *c*-axis are  $5.2 \times 10^{-6}$  and  $6.4 \times 10^{-6}$  K<sup>-1</sup>, respectively, and the *c*-axis approximately 20 % more expansible than *a*-axis (Hazen and Finger 1987). However, by fitting a “linearized” third-order high-temperature BM-EoS by using the unit-cell parameters data of beryl at high pressure and high temperature in this study and following the procedure implemented in the EosFit 5.2 program (Angel 2000), we obtained that

the axial thermal expansivities of beryl at ambient conditions along *a*-axis and *c*-axis are  $(4.6 \pm 1.1) \times 10^{-6}$  and  $(-2.6 \pm 0.4) \times 10^{-6}$  K<sup>-1</sup>, respectively. This is very consistent with previous room-pressure and high-temperature experimental study of beryl, which shows that beryl exhibits extreme anisotropic thermal expansion: The axial thermal expansion values at ambient conditions are  $(2.6 \pm 0.1) \times 10^{-6}$  and  $(-2.9 \pm 0.4) \times 10^{-6}$  K<sup>-1</sup> along *a*-axis and *c*-axis, respectively (Morosin 1972). Afterward, through the theoretical calculation method, Schlenker et al. (1977) also reported that the axial thermal expansivities of beryl at ambient conditions along *a*-axis and *c*-axis are  $(2.6 \pm 0.1) \times 10^{-6}$  and  $(-3.1 \pm 0.3) \times 10^{-6}$  K<sup>-1</sup>, respectively, which is also very consistent with the results of Morosin (1972) and this study. The possible reasons for the extreme anisotropy of thermal expansion in beryl are as follow. In all silicate structures determined at high temperatures, the Si tetrahedral volume is unchanged with increasing temperature. Furthermore, rigid groups of Si tetrahedra such as the six-member ring in beryl often display thermal contraction as a result of increased bridging-oxygen vibration amplitudes while Si–O distances remain constant (Hazen and Finger 1982). However, Be tetrahedral ring is expected to undergo a moderate linear expansion, on the basis of the observed relationship between bond thermal expansion and Pauling bond strength (Hazen and Finger 1982). In the (001) plane in beryl, thermal expansion is constrained by the “shrinking” Si tetrahedral rings, but modest expansion is possible parallel to *c* because of the expansion of Be tetrahedral (Hazen and Finger 1982).

It should also be pointed out that the sign of axial thermal expansion values of the *c*-axis for beryl is negative just at low temperatures (about below 600 K) (Morosin 1972; Schlenker et al. 1977). The results of Morosin (1972) show that the axial thermal expansion value of the *c*-axis for beryl decreases from a value of  $(-2.9 \pm 0.4) \times 10^{-6}$  K<sup>-1</sup> near room temperature to zero near 600 K and then increases and attains a value of  $(1.7 \pm 0.2) \times 10^{-6}$  K<sup>-1</sup> in the region above 700 K. This is very similar to the results by Schlenker et al. (1977), which also show a change in sign of axial thermal expansion values of the *c*-axis at about 650 K. We also calculated the axial thermal expansivities of beryl at high temperature along *c*-axis using the unit-cell parameters data of beryl at high pressure and high temperature in this study and obtained the axial thermal expansivities of beryl along *c*-axis at 450, 600, and 750 K are  $(-1.5 \pm 0.3) \times 10^{-6}$ ,  $(-0.3 \pm 0.1) \times 10^{-6}$ , and  $(1.0 \pm 0.2) \times 10^{-6}$  K<sup>-1</sup>, respectively, which also show a change in sign for the *c*-axis thermal expansion coefficient at about 650 K in this study (Fig. 9). Therefore, the result in this study about the change in sign of axial thermal expansion values of the *c*-axis for beryl at high temperature is very consistent with the previous studies (Fig. 9) (Morosin 1972; Schlenker et al. 1977).

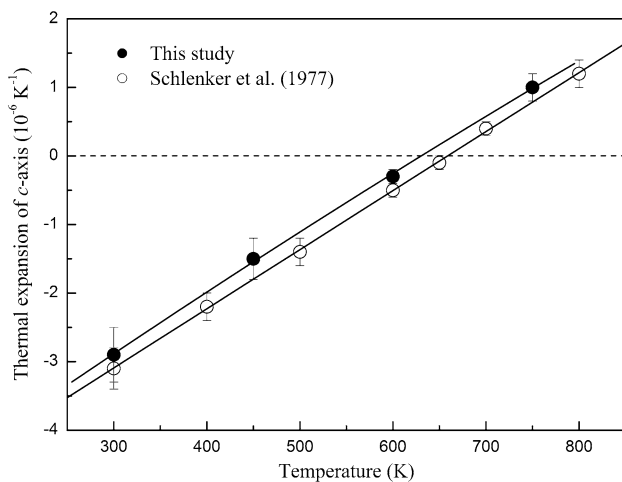


**Fig. 9** Axial thermal expansion coefficient of *c*-axis as a function of temperature at room pressure in this study compared with previous study (Schlenker et al. 1977)

## Conclusions

The single-crystal X-ray diffraction measurements at room temperature and high pressure, and the powder X-ray diffraction measurements at high temperature and high pressure, have been carried out on beryl in this study. Using the room-temperature BM-EoS, we have obtained the elastic parameters of beryl from single-crystal X-ray diffraction experiments at high pressure. Furthermore, the thermoelastic properties of beryl from powder X-ray diffraction experiments have been derived by using the *P*–*V*–*T* data set by high-temperature BM-EoS. The zero-pressure volume, isothermal bulk modulus, the temperature derivative of the bulk modulus, and thermal expansion coefficient were obtained. In addition, these elastic properties determined from two different approaches (single-crystal X-ray diffraction and powder X-ray diffraction experiments) show excellent agreements with each other. Furthermore, we found that beryl shows anisotropic elasticity along the *a*-axis and the *c*-axis with increasing pressure, and almost isotropic elasticity along the *a*-axis and the *c*-axis with increasing temperature under pressure. And we also observed that beryl exhibits anisotropic thermal expansion at ambient conditions: The axial thermal expansivities at ambient conditions of beryl along *a*-axis and *c*-axis are  $(4.6 \pm 1.1) \times 10^{-6}$  and  $(-2.6 \pm 0.4) \times 10^{-6} \text{ K}^{-1}$ , respectively. Our data provide a direct assessment of thermoelastic behavior of beryl at simultaneously high pressure and high temperature.

**Acknowledgments** The authors would like to thank Prof. Abby Kavner for the editorial handling, two anonymous reviewers for the constructive comments and suggestions, and Su-ying Chien at the

Center for High Pressure Science and Technology Advanced Research for her help in English improvements of the manuscript. This work was supported by the National Natural Science Foundation of China (Grant No. 41374107), the youth innovative technology talents program of Institute of Geochemistry, Chinese Academy of Sciences (2013, to Dawei Fan), the western doctor special fund of the West Light Foundation of Chinese Academy of Sciences (2011, to Dawei Fan). The high-temperature and high-pressure powder X-ray diffraction experiments were taken at the High Pressure Experiment Station (4W2), Beijing Synchrotron Radiation Facility (BSRF). The room-temperature and high-pressure single-crystal X-ray diffraction experiments were taken at the BL15U1 of the Shanghai Synchrotron Radiation Facility (SSRF).

## References

- Adamo I, Gatta GD, Rotiroli N, Diella V, Pavese A (2008) Gemmological investigation of a synthetic blue beryl: a multi-methodological study. *Miner Mag* 72:799–808
- Aines RD, Rossman GR (1984) The high-temperature behaviour of water and carbon dioxide in cordierite and beryl. *Am Miner* 69:319–327
- Andersson LO (2006) The position of  $\text{H}^+$ ,  $\text{Li}^+$  and  $\text{Na}^+$  impurities in beryl. *Phys Chem Miner* 33:403–416
- Angel R (2000) Equation of state. *Rev Miner Geochem* 41:35–60
- Angel RJ, Bujak M, Zhao J, Gatta GD, Jacobsen SD (2007) Effective hydrostatic limits of pressure media for high-pressure crystallographic studies. *J Appl Crystallogr* 40:26–32
- Artoli G, Rinaldi R, Ståhl K, Zanazzi PF (1993) Structure refinements of beryl by single-crystal neutron and X-ray diffraction. *Am Miner* 78:762–768
- Aurisicchio C, Fioravanti G, Grubessi O, Zanazzi PF (1988) Reappraisal of the crystal chemistry of beryl. *Am Miner* 73:826–837
- Barton MD (1986) Phase equilibria and thermodynamic properties of minerals in the  $\text{BeO}$ – $\text{Al}_2\text{O}_3$ – $\text{SiO}_2$ – $\text{H}_2\text{O}$  (BASH) system, with petrologic applications. *Am Miner* 71:277–300
- Brown GE Jr, Mills BA (1986) High-temperature structure and crystal chemistry of hydrous alkali-rich beryl from the Harding pegmatite, Taos County, New Mexico. *Am Miner* 71:547–556
- Burt DM (1978) Multisystems analysis of beryllium mineral stabilities: the system  $\text{BeO}$ – $\text{Al}_2\text{O}_3$ – $\text{SiO}_2$ – $\text{H}_2\text{O}$ . *Am Miner* 63:664–676
- Čemić L, Franz G, Langer K (1986) Experimental determination of melting relationships of beryl in the system  $\text{BeO}$ – $\text{Al}_2\text{O}_3$ – $\text{SiO}_2$ – $\text{H}_2\text{O}$  between 10 and 25 kbar. *Miner Mag* 50:55–61
- Charoy B (1999) Beryllium speciation in evolved granitic magmas: phosphates versus silicates. *Eur J Miner* 11:135–148
- Charoy B, De Donato P, Barres O, Pinto-Coelho C (1996) Channel occupancy in alkali-poor beryl from Serra Branca (Goias, Brazil): spectroscopic characterization. *Am Miner* 81:395–403
- de Almeida Sampaio Filho H, Sighinolfi G, Galli E (1973a) Contribution to crystal chemistry of beryl. *Contrib Miner Petr* 38:279–290
- de Almeida Sampaio Filho H, Sighinolfi GP, Galli E (1973b) Contribution to the crystal chemistry of beryl. *Contrib Miner Petrol* 38:270–290
- Dera P, Zhuravlev K, Prakapenka V, Rivers ML, Finkelstein GJ, Grubor-Urosevic O, Tschauner O, Clark SM, Downs RT (2013) High-pressure single-crystal micro-X-ray diffraction ( $\text{SC}\mu\text{XRD}$ ) analysis with GSE\_ADA/RSV software. *High Press Res* 33:466–484
- Evensen JM, London D, Wendlandt RF (1999) Solubility and stability of beryl in granitic melts. *Am Miner* 84:733–745
- Fan DW, Zhou WG, Wei SY, Liu YG, Ma MN, Xie HS (2010) A simple external resistance heating diamond anvil cell and its

- application for synchrotron radiation x-ray diffraction. *Rev Sci Instrum* 81:053903
- Fei YW, Ricolleau A, Frank M, Mibe K, Shen GY, Prakapenka V (2007) Toward an internally consistent pressure scale. *Proc Natl Acad Sci* 104:9182–9186
- Gatta GD, Nestola F, Bromiley GD, Mattauch S (2006) The real topological configuration of the extra-framework content in alkali-poor beryl: a multi-methodological study. *Am Miner* 91:29–34
- Gibbs GV, Breck DW, Meagher EP (1968) Structural refinement of hydrous and anhydrous synthetic beryl  $\text{Al}_2(\text{Be}_3\text{Si}_6)\text{O}_{18}$  and emerald,  $\text{Al}_{1.9}\text{Cr}_{0.1}(\text{Be}_3\text{Si}_6)\text{O}_{18}$ . *Lithos* 1:275–285
- Goldman DS, Rossman GR, Parkin KM (1978) Channel constituents in beryl. *Phys Chem Miner* 3:225–235
- Hammersley AP, Svensson SO, Hanfland M, Fitch AN, Hausermann D (1996) Two-dimensional detector software: from real detector to idealized image or two-theta scan. *High Press Res* 14:235–248
- Hawthorne FC, Černý P (1977) The alkali-metal positions in Cs–Li beryl. *Can Miner* 15:414–421
- Hazen RM, Finger LW (1982) Comparative crystal chemistry. Wiley, New York
- Hazen RM, Finger LW (1987) High-temperature crystal chemistry of phenakite ( $\text{Be}_2\text{SiO}_4$ ) and chrysoberyl ( $\text{BeAl}_2\text{O}_4$ ). *Phys Chem Miner* 14:426–434
- Hazen RM, Au AY, Finger LW (1986) High-pressure crystal chemistry of beryl ( $\text{Be}_3\text{Al}_2\text{Si}_6\text{O}_{18}$ ) and euclase ( $\text{BeAlSiO}_4\text{OH}$ ). *Am Miner* 71:977–984
- Holland TJB, Redfern SAT (1997) Unit cell refinement from powder diffraction data: the use of regression diagnostics. *Miner Mag* 61:65–77
- Kolesov BA, Geiger CA (2000) The orientation and vibrational states of  $\text{H}_2\text{O}$  in synthetic alkali-free beryl. *Phys Chem Miner* 27:557–564
- Larson AC, Von Dreele RB (2000) GSAS general structure analysis system operation manual. Los Alamos Natl Lab LAUR 86–748:1–179
- Le Bail A, Duroy H, Fourquet JL (1988) Ab initio structure determination of  $\text{LiSbWO}_6$  by X-ray powder diffraction. *Mater Res Bull* 23:447–452
- Mao HK, Bell PM, Shaner JW, Steinberg DJ (1978) Specific volume measurements of Cu, Mo, Pd, and Ag and calibration of the ruby R1 fluorescence pressure gauge from 0.06 to 1 Mbar. *J Appl Phys* 49:3276–3283
- Morosin B (1972) Structure and thermal expansion of beryl. *Acta Cryst B* 28:1899–1903
- Pankrath R, Langer K (2002) Molecular water in beryl,  $^{\text{VI}}\text{Al}_2[\text{Be}_3\text{Si}_6\text{O}_{18}] \cdot n\text{H}_2\text{O}$ , as a function of pressure and temperature: an experimental study. *Am Miner* 87:238–244
- Piermarini GJ, Block S, Barnett JD (1973) Hydrostatic limits in liquids and solids to 100 kbar. *J Appl Phys* 44:5377–5382
- Prencipe M, Nestola F (2005) Quantum-mechanical modeling of minerals at high pressure. The role of the Hamiltonian in a case study: the beryl ( $\text{Al}_4\text{Be}_6\text{Si}_{12}\text{O}_{36}$ ). *Phys Chem Miner* 32:471–479
- Prencipe M, Scanavino I, Nestola F, Merlini M, Civalleri B, Bruno M, Dovesi R (2011) High-pressure thermo-elastic properties of beryl ( $\text{Al}_4\text{Be}_6\text{Si}_{12}\text{O}_{36}$ ) from ab initio calculations, and observations about the source of thermal expansion. *Phys Chem Miner* 38:223–239
- Qin S, Liu J, Li HJ, Zhu XP, Li XD (2008) *In-situ* high-pressure X-ray diffraction of natural beryl. *Chin J High Press Phys* 22:1–5 (in chinese)
- Schlenker JL, Gibbs GV, Hill EG, Crews SS, Myers RH (1977) Thermal expansion coefficients for indialite, emerald, and beryl. *Phys Chem Miner* 1:243–255
- Sheriff BL, Grundy DH, Hartman JS, Hawthorne FC, Černý P (1991) The incorporation of alkalis in beryl: multi-nuclear MAS NMR and crystal structure study. *Can Miner* 29:271–285
- Toby BH (2001) EXPGUI, a graphical user interface for GSAS. *J Appl Crystallogr* 34:210–213
- Wood DL, Nassau K (1968) The characterization of beryl and emerald by visible and infrared absorption spectroscopy. *Am Miner* 53:777–800
- Yoon HS, Newnham RE (1973) The elastic properties of beryl. *Acta Cryst A* 29:507–509